Electronic structure orientation as a map of in-plane antiferroelectricity in β'-In_2Se_3

Joseph L. Spellberg,[1,2] Lina Kodaimati,[1] Prakriti P. Joshi,[2]
Nasim Mirzajani,[1,2] Liangbo Liang,[3] and Sarah B. King[1,2]

[1] *Department of Chemistry, University of Chicago, 929 E 57th Street, Chicago, IL 60637*
[2] *James Franck Institute, University of Chicago, 929 E 57th Street, Chicago, IL 60637*
[3] *Center for Nanophase Materials Sciences, Oak Ridge National Laboratory, Oak Ridge, TN 37831*

(Dated: January 19, 2024)

Antiferroelectric (AFE) materials are excellent candidates for sensors, capacitors, and data storage due to their electrical switchability and high-energy storage capacity. However, imaging the nanoscale landscape of AFE domains is notoriously inaccessible, which has hindered development and intentional tuning of AFE materials. Here, we demonstrate that polarization-dependent photoemission electron microscopy (PD-PEEM) can resolve the arrangement and orientation of in-plane AFE domains on the nanoscale, despite the absence of a net lattice polarization. Through direct determination of electronic transition orientations and analysis of domain boundary constraints, we establish that antiferroelectricity in β'-In_2Se_3 is a robust property from the nanometer to the 10s µm scale, confirming β'-In_2Se_3 is an excellent candidate for applications requiring control of AFE polarization. Ultimately, the understanding of nanoscale AFE domain organization presented here opens the door to new investigations in the influence of domain formation and orientation on charge transport and dynamics.

INTRODUCTION

Antiferroelectric (AFE) materials, featuring antiparallel, switchable, permanent dipoles [1, 2] are excellent for energy-dense capacitors [3] and memory devices with robust storage capabilities [4, 5]. Rational design and development of AFE materials, however, has wrestled with the challenge of imaging AFE domains on the nanoscale to determine, for example, how nanoscale and mesoscale electronic properties arise from atomic structure [6]. Given the lack of a net permanent dipole in AFE materials, piezoresponse force microscopy (PFM) offers little to no domain contrast, depending on a material's electrostriction coefficient. Furthermore, PFM cannot provide information on the orientation of domains, only that domains are different [7–9]. Ferroic domains, such as those in AFE materials, are commonly on the order of 10s-100s of nm [10, 11], below the optical diffraction limit, making ferroic domains challenging to study with optical microscopy. These challenges have not only inhibited material development, but also made it impossible to determine how AFE domain formation impacts other critical properties, such as excited state dynamics, known to be important in other ferroic materials [12]. Here, we introduce how polarization-dependent photoemission electron microscopy (PD-PEEM) can image in-plane AFE domains, demonstrating a new way to resolve in-plane AFE domain structure on the nanoscale, and apply this technique to β'-In_2Se_3.

Indium(III) selenide (In_2Se_3) is a semiconductor with a complex phase diagram that includes two-dimensional van der Waals (vdW) ferroelectric and antiferroelectric phases [13–20]. The metastable β' phase, which forms in thin-film samples due to substrate interactions when cooling from the high temperature β phase [13–15, 21–23], exhibits in-plane ferroelasticity and antiferroelectricity down to the monolayer limit [1, 7, 24].

Antiferroelectricity occurs in β'-In_2Se_3 due to a nanostripe superstructure that forms as it cools from the hexagonal, high temperature β phase [13, 21]. The nanostripes form along any one of three symmetrically-equivalent [11$\bar{2}$0] lattice vectors, defined by the structure of the symmetric high-temperature β phase, and have been observed with scanning tunneling microscopy (STM), scanning transmission electron microscopy (STEM), and electron diffraction [7, 21, 27, 28]. Antiferroelectricity in β'-In_2Se_3 was confirmed by Xu *et al.* [24] who showed that adjacent nanostripes are composed of anti-parallel atomic displacements resulting in the lack of a net permanent dipole moment (Figure 1(a))[19, 24]. Optical birefringence and optical absorption microscopy of β'-In_2Se_3 show characteristic cross-hatched patterns that have been suggested to be domains of similarly oriented nanostripes [7, 21, 24]. However, confirming the relationship between these μm-scale domains and the antiferroelectric atomic distortions has been challenging, as optical birefringence does not allow for direct measurement of domain orientation nor has has neither sufficient spatial resolution to clearly image domain structure.

In this paper, we show how PD-PEEM can image the AFE domains of β'-In_2Se_3 on the nanoscale by directly measuring the energy- and polarization-dependent transition dipole moment. Previous PEEM studies have successfully imaged ferroelectric and ferromagnetic domains, but these studies have relied on X-ray and extreme UV excitation to access core levels and do not probe optical transitions as in this work [29–32]. Despite having zero net permanent dipole, the small atomic distortions that give rise to the AFE nature of β'-In_2Se_3 lead to

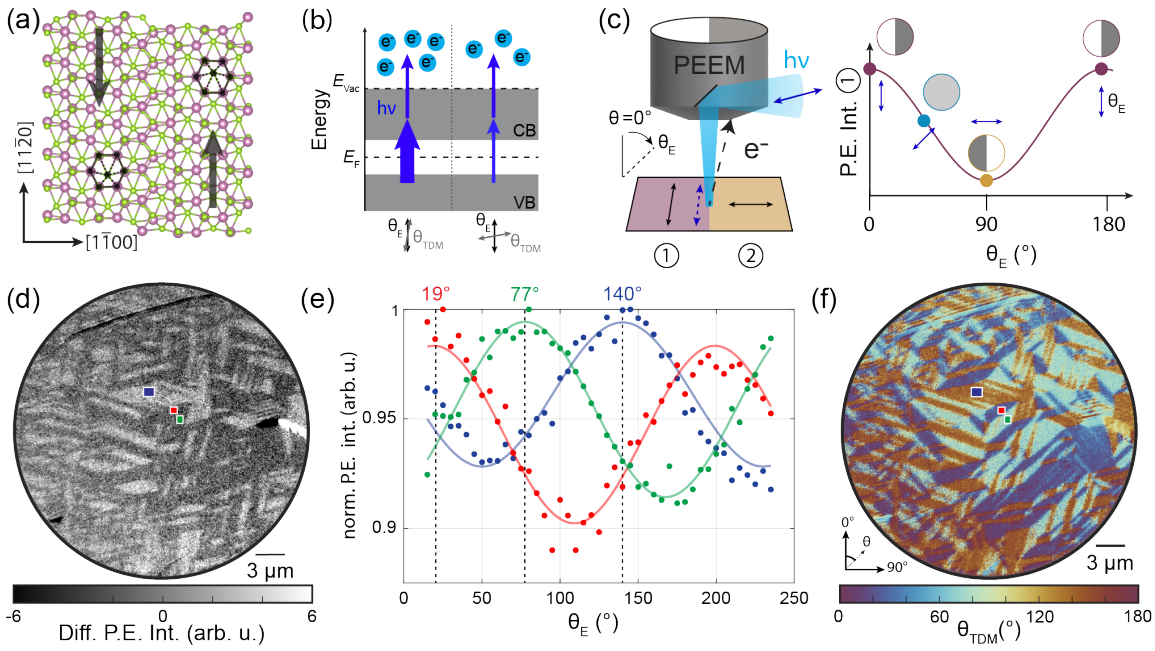

FIG. 1. (a) Atomic structure of a supercell of β'-In_2Se_3, where green indicates Se and purple indicates In. Two adjacent, antiparallel nanostripes are depicted with the gray arrows indicating their atomic displacement directions. (b) Energy level diagram of polarization-dependent two-photon photoemission (2PPE) process. Variation in the alignment of the laser polarization (θ_E) with a material's local transition dipole moment (θ_{TDM}) results in the modulation of the number of photoemitted electrons. (c) Schematic of polarization-dependent photoemission microscopy (PD-PEEM) for spatially-dependent θ_{TDM} . White shading indicates maximum photoemission intensity and dark gray indicates minimum intensity. Rotation of θ_E modulates the PE intensity from domains with different atomic displacements and thereby different θ_{TDM}. (d) $I(\theta_E = 140°) - I(\theta_E = 50°)$ difference image from PD-PEEM with $h\nu = 3.1$ eV shows the modulated PE intensity from differently oriented domains of β'-In_2Se_3 (e) PE intensity vs laser polarization from the three regions indicated by the red, blue, and green rectangles in (d) showing 60° phaseshifts between domains, where 0° is vertical in the plane of the image and positive angles correspond to clockwise rotation as indicated in (c). Dots are integrated PE intensity which have been normalized to their maxima. Solid lines are fits to Equation 1 ($R^2_{red} = 0.94$, $R^2_{green} = 0.97$, $R^2_{blue} = 0.89$). (f) Map of θ_{TDM} parameter from Equation 1, fit to each pixel in the PD-PEEM data. The color bar [25, 26] shows three distinct domains resolved as blue, cyan, and brown. Maps of R^2 for pixel-by-pixel fitting are shown in Figure S5.

significant electronic structure modifications that can be observed with PD-PEEM. Our method identifies AFE domain orientation, achieves an approximately 8 fold enhanced resolution compared to standard optical birefringence, and allows the identification of AFE properties inaccessible to conventional optical microscopy. Using first-principles density functional theory (DFT), we calculate the photon-energy dependent transition dipole moments (TDM) and match our calculations with experimentally measured photon-energy dependent maps of TDM orientations. Analysis of the domain patterns observed in PD-PEEM and comparison to previous atomic imaging shows that the in-plane AFE nanostripes observed in STM and STEM directly combine to form the μm-scale domains observed in optical birefringence and that the AFE domains are robust across 10s of μm making β'-In_2Se_3 a promising candidate for applications requiring long range control over in-plane polarization [33]. This work opens up a new way to probe antiferroelectricity on the nanoscale and sets the stage for further investigations of the unique electronic structure at ferroic domain boundaries such as charge transport [12, 34], carrier lifetimes [35], and electrical properties [36].

RESULTS

Imaging Domains with PD-PEEM

Contrast in PD-PEEM arises from the dependence of photoemission (PE) intensity on the angle between the laser electric field polarization (θ_E) and material's local transition dipole moment (θ_{TDM}), shown schematically in Figure 1(b,c). This technique has been used previously to image the localized electronic states in black phosphorus [37] and polymer packing alignment [38]. The PE intensity is maximized at $\theta_E = \theta_{TDM}$, when θ_E is parallel to the θ_{TDM} and the relationship between PE intensity and θ_E is defined by

$$I_{PE}(\theta) = A\cos^2(\theta_E - \theta_{TDM}) + C, \quad (1)$$

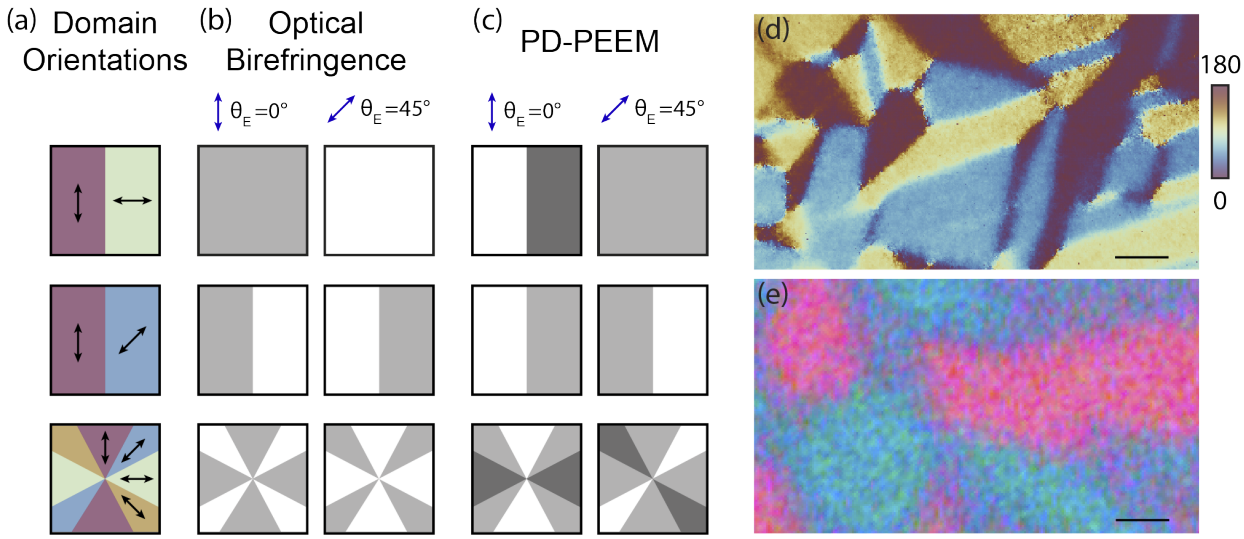

FIG. 2. (a) Schematic of different domain structures where the arrows indicate spatially variant θ_{TDM}. (b) Schematic of visualization of the same domains using optical birefringence for $\theta_{\mathrm{E}} = 0^{\circ}$ and $\theta_{\mathrm{E}} = 45^{\circ}$. Domains with perpendicular θ_{TDM} cannot be uniquely resolved. (c) Schematic of visualization of different domain orientations in PD-PEEM. All domain directions can be uniquely determined by rotation of θ_{E}. In both schematics, white indicates greater intensity measured at the detector and gray indicates less intensity. (d) θ_{TDM} map from PD-PEEM on a β'-In_2Se_3 flake with $h\nu = 3.1$ eV. Scale bar is 1 μm. (e) Optical birefringence image of β'-In_2Se_3 with the same scale as in (d).

where A is the amplitude of the modulation and C is the photoemission baseline. A detailed description of the optical selection rules of PD-PEEM can be found in Joshi *et al.* [37]. Incrementally rotating through the full 180° range of laser polarization we observe the domains of β'-In_2Se_3 by their polarization-dependent PE intensity. Figure S3 shows examples of PD-PEEM images of a β'-In_2Se_3 flake. A movie showing PE intensity with respect to rotating θ_{E} is included in the Supplementary Material. To better visualize the domains, Figure 1(d) shows the difference between PD-PEEM images recorded at $\theta_{\mathrm{E}} = 140^{\circ}$ and $\theta_{\mathrm{E}} = 50^{\circ}$, where bright regions correspond to $\theta_{\mathrm{TDM}} \approx 140^{\circ}$. Integrating over the three indicated regions of interest and fitting to equation 1, Figure 1(e), we identify three domain orientations offset from each other by approximately 60°, comprising a three-fold symmetric set of directions in the 180° range of unique θ_{E}.

By fitting the PE intensity of every pixel as a function of θ_{E}, we can directly map the local θ_{TDM} alignment. A θ_{TDM} map of β'-In_2Se_3 with $h\nu = 3.1$ eV (Figure 1(f)) shows the characteristic cross-hatch domain pattern seen previously in optical birefringence experiments [24]. Optical and AFM images of the same flake (Figure S4) show that the observed contrast does not originate from topographical features, but is due to local variations in electronic structure and domain orientation. There are predominantly three domain orientations ($\theta_{\mathrm{TDM,\ blue}} \approx 19^{\circ}$, $\theta_{\mathrm{TDM,\ cyan}} \approx 77^{\circ}$, and $\theta_{\mathrm{TDM,\ brown}} \approx 140^{\circ}$), each containing one of the regions of interest. This three-fold symmetry is consistent with domains of similarly oriented nanostripes, which can exist along one of the three symmetric $[11\bar{2}0]$ lattice vectors.

PD-PEEM provides two notable advantages for imaging domains with different θ_{TDM} in comparison to optical birefringence microscopy. First, there is a wider range of unique θ_{E} that results in observable contrast in PD-PEEM. Figure 2(a) schematically shows possible arrangements of domains in a material with in-plane polarization and Figures 2(b,c) show how these domains would be observed by optical birefringence and PEEM, respectively. The periodicity of intensity with respect to laser polarization for optical birefringence is 90° [39, 40]. This means that θ_{TDM} directions (which often correspond to the birefringent axis) cannot be determined uniquely with this method because two perpendicular orientations would equally rotate the incident light and produce the same image (Figure 2(b)). Similarly, domains oriented perpendicular to each other cannot be separately resolved, regardless of the incident polarization [40]. PEEM intensity, however, has 180° periodicity with respect to laser polarization meaning that all domain orientations can be uniquely identified. Therefore, PD-PEEM provides information regarding the alignment of domains that optical birefringence cannot resolve (2(c)). Second, electron imaging is bounded by a lower diffraction limit compared to imaging with photons, which allows the identification of features smaller than the optical diffraction limit [37]. A map of β'-In_2Se_3 domains from a zoomed-in field of view (Figure 2(d)) shows readily apparent small features

on the order of 100 nm that would be lost when imaging with a lower resolution technique such as optical microscopy (Figure 2(e)). The flake in Figure 2(e) is on a thick layer of SiO_2 to boost contrast while the PEEM experiments are conducted on Si substrates with native oxide. An example of both methods applied to the same flake is shown in Figure S6. Resolution cuts for the images in Figures 2(d) and (e) are shown in Figure S7 where we achieve an approximately 8 fold improvement over optical birefringence with PD-PEEM.

Energy-Dependent Transition Dipole Moment

To better understand the contrast mechanism enabling the observation of β'-In_2Se_3 domains with PD-PEEM, we performed DFT calculations to determine the frequency-dependent dielectric function and optical transition matrix of a supercell of β'-In_2Se_3. Using previously published atomic positions for a supercell of the AFE lattice measured experimentally [24], we calculated the band structure and TDM angle with respect to nanostripe direction for a range of excitation energies from 1.3 to 3.4 eV, corresponding to across band gap transitions in the PEEM measurements. Although β'-In_2Se_3 has no net permanent dipole, DFT confirms that there is polarization anisotropy in across band gap transitions. The magnitude of this anisotropy is quantified by the linear optical dichroism as discussed in the Supplementary Material. The calculated optical dichroism, the gray trace in Figure 3, varies for different excitation energies, but is nonzero across the calculated range with a mean of approximately 0.3. The small distortions which give rise to the nanostripe superstructure in β'-In_2Se_3 create electronic structure anisotropy can be probed with polarization-dependent photoexcitation. In addition to confirming the non-zero dichroism, our calculations also predict that the transition dipole moment is oriented either parallel or perpendicular to the nanostripe direction, depending on the excitation energy. The black points in Figure 3 show that these are the only directions that the TDM orientation can take. There is not a particular energy where the TDM angle changes, but rather the orientation switches back and forth. Polar plots showing absorption intensity vs polarization angle for two excitation energies are shown in the inset. Absorption of $h\nu = 2.4$ eV (orange curve) is oriented along the nanostripe direction and has relatively strong dichroism and absorption of $h\nu = 3.05$ eV (blue curve) is perpendicular to the nanostripe direction and has much weaker, but still nonzero, dichroism.

This binary selection of allowed values for θ_{TDM} is consistent with the 180° periodicity observed in the PD-PEEM response. The laser aligns with the θ_{TDM} only once for each 180° rotation and suggests that θ_{TDM} is restricted to be oriented parallel or perpendicular to the stripe direction (Figure S8), which is corroborated by optical dichroism and birefringence experiments [7, 21, 24].

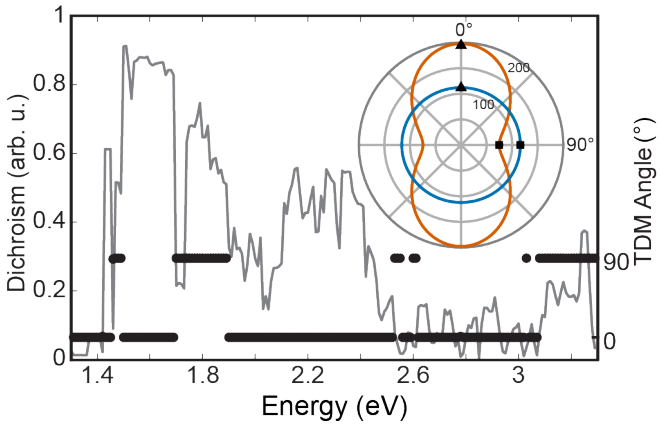

FIG. 3. Optical dichroism and transition dipole moment (TDM) angle vs $h\nu$ for across band gap transitions in β'-In_2Se_3. Dichroism (gray trace) is nonzero across the entire calculated range, but is non-uniform. TDM angle (black points) is always parallel (0°) or perpendicular (90°) to the nanostripe direction. Inset: Polar plot of transition intensity for $h\nu = 2.40$ eV (orange) and $h\nu = 3.05$ eV (blue). Distance from origin is the strength of photoabsorption and angle is polarization orientation. Triangles indicate parallel to nanostripes and squares are perpendicular.

We confirmed the energy-dependence of the transition dipole moment orientation and dichroism experimentally. Figures 4(a,b) show maps from two polarization-dependent PEEM experiments on a β'-In_2Se_3 flake that was illuminated with 3.06 eV and 2.40 eV photons, respectively. These excitation energies result in two and three photon processes (Figure S9). While the same domain patterns are observed in both images, θ_{TDM} measured in each domain is phase-shifted by $\sim 90°$ between the two measurements, Figure 4(c), in agreement with the DFT prediction. The PE response for both excitation energies has low dichroism, but it is stronger for $h\nu = 2.40$ eV, consistent with the trend predicted by DFT. Pixel-by-pixel analysis of the dichroism confirms this to be true across the entire flake (Figure S10). While limitations on DFT's energetic accuracy prevents our energy-dependent results from being used to assign lattice directions, the agreement between experiment and theoretical calculations suggest that the across band gap transition dipole moments in β'-In_2Se_3 are preferentially oriented parallel or perpendicular to the nanostripe direction, depending on $h\nu$ and which electronic states are coupled with a photon.

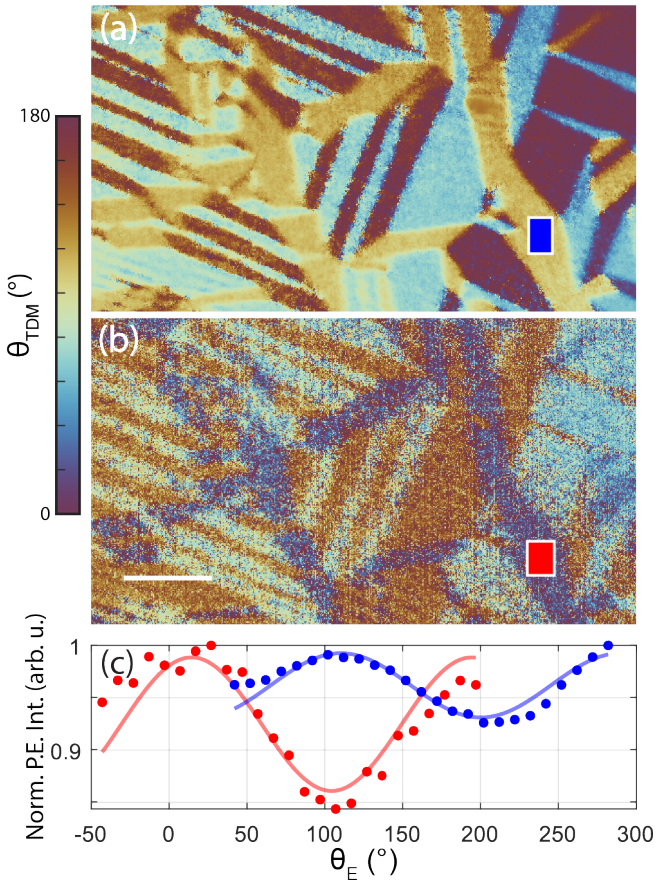

FIG. 4. Maps of θ_{TDM} for β'-In_2Se_3 illuminated with (a) $h\nu$ = 3.06 eV and (b) $h\nu$ = 2.40 eV. (c) Traces of PE intensity vs θ_{E} for the indicated regions shows a $\sim 90°$ phaseshift between the experiments. 0° is vertical in the plane of the image and positive angles correspond to clockwise rotation as shown in figure 1(c). Dots are normalized integrated PE intensity and solid lines are fits to Equation 1 (R^2_{blue} = 0.81 and R^2_{red} = 0.87). Scale bar is 3 μm.

Domain Boundary Orientations

To connect the optical axes identified by the energy-dependent measurements to the atomic scale distortions in the β'-In_2Se_3 supercell and the calculated TDM angles in the lattice coordinate frame, we analyzed the geometry of domains and domain boundary arrangements observed in the PD-PEEM data. Previous atomic scale STEM imaging of individual domain walls in β'-In_2Se_3 established that the formation of boundaries between AFE domains is governed by three geometric rules, which we analyze and confirm in our experiments by measuring boundary orientations across the entire field of view (Figures 5(a), S11, and S12). Namely, (1) nanostripes form along the [11$\bar{2}$0] lattice directions, (2) domain walls can form in six discrete directions along either the [11$\bar{2}$0] or [1$\bar{1}$00] lattice vectors, and (3) domain boundaries always bisect the angle formed by adjacent nanostripes [7, 24]. These three rules, illustrated schematically in Figure 5(b), establish both which domain shapes are possible and how nanostripes can and cannot orient within domains. A complete geometric analysis describing how these rules extend to larger spatial scales and how domains and domain boundaries can be combined to make different geometric patterns is included in the Supplementary Materials (Figures S13-S16). Here, we show that the domain pattern observed in PD-PEEM is fully consistent with the geometry defined by atomic scale nanostripes, directly connecting the domains resolved over a 30 μm field of view to the atomic distortions in the lattice that give rise to antiferroelectricity.

We measured the angles of the domain wall boundaries of the flake discussed in Figure 1 across the entire 30 μm field of view (Figure S11) and constructed a histogram of the angle of each domain boundary with respect to the coordinate system of the PEEM image, Figure 5(c). The angles of the domain walls are grouped into six discrete orientations, spaced by $\sim 30°$. Each specific domain wall direction corresponds to a unique pair of domain orientations. For example, all domain walls with an angle of about 20° (cluster A, indicated in yellow), correspond to boundaries between domains with $\theta_{\mathrm{TDM}} \approx 80°$ and 140° (resolved as cyan and brown, respectively, in Figures 1(f) and 5(a)). Similarly, every other boundary orientation uniquely corresponds to a pair of domains (Figure 5(d)). The histogram clusters can be divided into perpendicular pairs. For example, boundary classes A and D separate the same two domain types ($\theta_{TDM} \approx 80°$ and 140°) and are oriented about 90° from each other. The same correspondence between perpendicular domain boundaries is true for the other four directions. These findings are all consistent with two perpendicular, three-fold symmetric set of boundary orientations ([11$\bar{2}$0] or [1$\bar{1}$00]).

We also identify the rotation of θ_{TDM} between adjacent domains, $\Delta\theta_{TDM}$, to be 60° or 120° and the angle is bisected by their boundary, as illustrated in Figure 5(d). These are the same angles that nanostripes form at boundaries, as determined by STEM [7], confirming that the atomic nanostripes directions and θ_{TDM} values have equivalent relationships to the boundaries that contain them. Therefore, these two quantities must be aligned along the same two axes. The shape and orientation of a particular domain restricts the nanostripe direction and θ_{TDM} that it can contain (discussed in detail in the supplemental information). From this we can confirm that the two optical axes identified with the energy-dependent measurement are oriented parallel and perpendicular to the nanostripe direction, further supporting the DFT calculations (Figure S17).

Each of the three 'rules' for β'-In_2Se_3 AFE domains are rigorously consistent for the μm-scale domains observed with PD-PEEM across the entire 30 μm field of view and across multiple flakes (Figure S12). While derived from

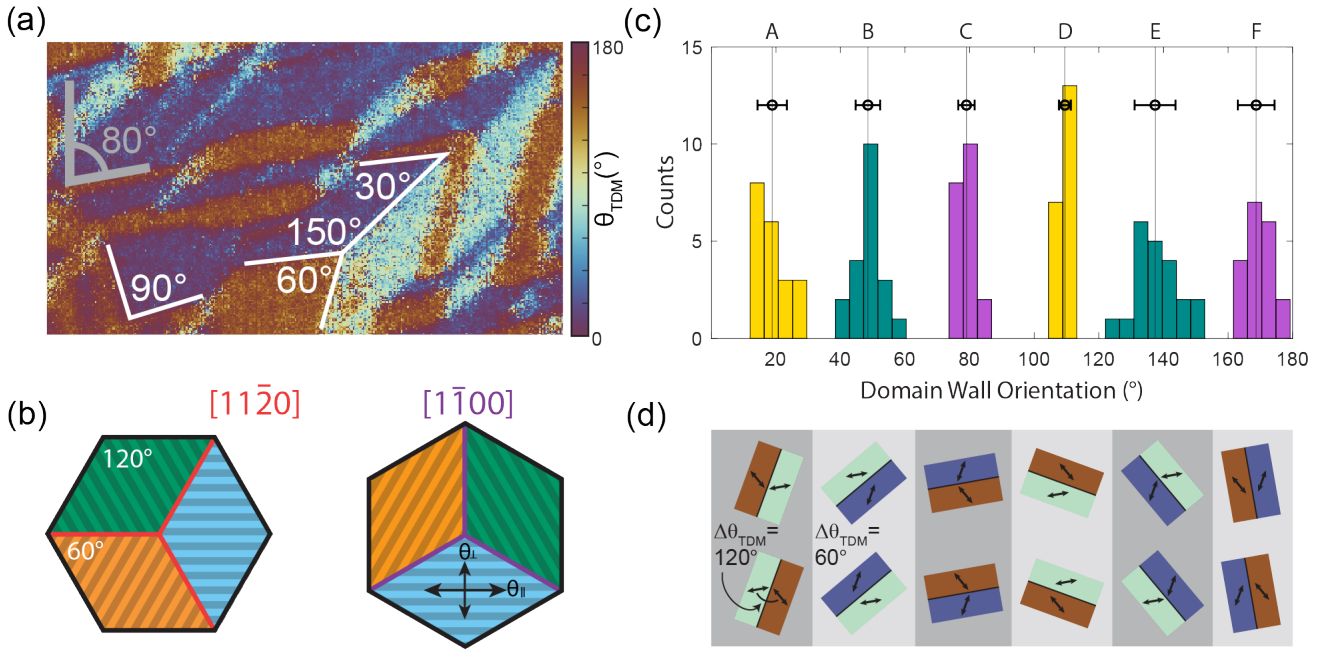

FIG. 5. (a) Region from the θ_{TDM} map in Figure 1(f) with a selection of domain boundaries and interior angles indicated. Domain boundary angles are measured with respect to the image vertical axis according to the coordinate system defined in Figure 1(f); white lines indicate domain interior angles. (b) Schematic of domain walls along the [11$\bar{2}$0] and [1$\bar{1}$00] directions. Orange, blue, and green regions indicate domains with different nanostripe orientations, respective to the lab frame, which are indicated by shaded lines. $\theta_{\perp}$ and $\theta_{\parallel}$ indicate possible θ_{TDM} directions with respect to nanostripe directions. (c) Histogram of domain wall orientations from PD-PEEM data shown in Figure 1(f). Black circles indicate the mean domain wall orientation and error of each cluster. Comparing all the differences between each point in adjacent groups, the average rotation between domain boundaries is $30 \pm 6^{\circ}$. Bar colors indicate groupings according to which pair of domains are divided according to experimentally measured values of θ_{TDM}. Yellow indicates boundaries that divide $\theta_{\mathrm{TDM}} \approx 77^{\circ}$ and 140°, green indicates boundaries between $\theta_{\mathrm{TDM}} \approx 19^{\circ}$ and 77°, and purple indicates boundaries between $\theta_{\mathrm{TDM}} \approx 19^{\circ}$ and 140°. (d) Domains separated by each boundary orientation in (a) according to θ_{TDM} directions measured with PD-PEEM. Double headed arrows indicate transition dipole moment direction and always form an angle that is bisected by the domain boundary. Shaded background indicates the same value of $\Delta\theta_{TDM}$.

atomic scale images, these 'rules' show impressive fidelity on the scale of 10s of μms indicating β'-In_2Se_3's utility in applications requiring long range control of in-plane polarization and domain structure [33]. While we cannot specify which optical axis corresponds to which lattice vector, the energy-dependent measurement in conjunction with the shape analysis confirms that the electronic structure orientation is dictated by the atomic distortions such that θ_{TDM} is always parallel or perpendicular to the nanostripe direction.

DISCUSSION

In this work we use PD-PEEM to image the AFE domain structure of β'-In_2Se_3 over multiple length scales from 10s of nm to 10s of μm, and show that AFE domains result from regions with aligned nanostripe superstructures. This technique successfully images in-plane AFE domains with sub-100 nm spatial resolution to resolve structures and polarization directions that are inaccessible via other methods. The domain structure of β'-In_2Se_3 is highly robust and shows an impressive degree of fidelity across large spatial regions and multiple samples, indicating that β'-In_2Se_3 may be a viable candidate for 2D memory storage and other applications requiring control over in plane polarization. Additionally, β'-In_2Se_3, with its photon-energy dependent electronic transition orientation, is an intriguing candidate for optical filtering devices and photonics applications.

This photon-energy dependent orientation creates both challenges and opportunities in the future study of β'-In_2Se_3. Since the birefringence of a material is related to the optical transition dipole moment [39], we note that care must be taken when using optical measurements to study polarization or lattice directions in β'-In_2Se_3 given the variation in θ_{TDM} as a function of photon energy. When broadband white light in particular is used, the measured angle of maximum photoabsorption will not necessarily align with the direction of AFE polarization;

rather, the measured angle will represent a convolution of the simultaneous responses of multiple photon energies. This is further complicated by the non-uniform relationship between optical dichroism and excitation energy. However, in experiments with precise excitation energy, β'-In_2Se_3 presents an exciting platform for the investigation of anisotropic electronic structure and properties. The findings presented in this work show that PD-PEEM can accurately resolve domains even when there is no net lattice polarization. Even minor distortions, like those that form the nanostripes of β'-In_2Se_3, lead to electronic structure changes that are sufficiently strong to be readily resolved in PD-PEEM. Our results exemplify the many opportunities for using PD-PEEM in studying the physics of in-plane ferroelectrics, antiferroelectrics, and other domain structures of materials.

MATERIALS AND METHODS

Sample Preparation

In_2Se_3 flakes were mechanically exfoliated from a bulk crystal grown by chemical vapor transport (2D Semiconductors) in N_2 atmosphere. The flakes were transferred via PDMS stamp [41] onto Si with native oxide substrates and annealed on a hot plate at 300-350°C for 30 minutes. Upon cooling to room temperature, the β' phase is produced (Figures S1 and S2). Samples were then observed in cross-polarized optical microscopy to verify the presence of AFE domains on the flakes. Subsequent characterization with atomic force microscopy (Bruker MM8, ScanAsyst) and Raman Microspcopy (HORIBA LabRAM HR Evolution confocal Raman microscope) determined flakes thicknesses and phases, respectively. All flakes discussed in this work have thicknesses of a few 100s of nm.

Photoemission Electron Microscopy

Photoemission experiments were conducted in a photoemission electron microscope (Focus GmbH, Scienta Omicron GmbH). Laser illumination is directed to into the chamber through a thin film polarizer and a $\lambda/2$ waveplate on a rotational stage. In the chamber, the laser beam reflects off a Rh mirror to be incident on the sample at 4° from the surface normal, causing the polarization to be effectively in the plane of the sample. Illumination is from an optical parametric chirped pulse amplifier (Class 5 Photonics; Figures 1, 5, S3, S11, S12(a,b), S16(f) and Movie S1), a home-built nonlinear optical parametric amplifier (Figures 2(d), 4(a), S6(c), S7(a), S9, S10, S12(e), and S17(a)), or the second harmonic of a 1035 nm fundamental (Coherent Monaco; Figures 4(b) and S17(b)). All experiments were conducted with 4 MHz repetition rates.

DFT

DFT calculations were performed using the Vienna *ab initio* simulation package (VASP, version 5.4.4), where the projected augmented wave (PAW) method was used for pseudopotentials[42, 43], and the electron exchange-correlation functional was chosen as the generalized gradient approximation (GGA) of Perdew, Burke and Ernzerhof (PBE) [44]. The monolayer antiferroelectric nanostripe structure [24] was fully relaxed by the conjugate gradient scheme until the maximum force was less than 0.01 eV/Å on each atom. The total energy was converged to 10^{-6} eV. The energy cutoff of the plane waves was chosen as 350 eV. The kpoint sampling in the Brillouin Zone (BZ) corresponds to Γ-centered $1 \times 12 \times 1$ k-grid. Additionally, a vacuum region of approximately 18 Å in the z direction was used to avoid spurious interactions between the neighboring cells. The optimized in-plane lattice constants are $a = 27.668$ Å and $b = 4.076$ Å, while c is fixed to 25Å. Based on the nanostripe structure, a $1 \times 7 \times 1$ supercell was built, for which only the Γ point in the BZ was considered while other parameters are unchanged. For such a supercell, we computed its frequency-dependent dielectric function using VASP, which also generates the optical transition matrix elements between any valence and conduction states. These optical transition matrix elements enable us to obtain the transition dipole moment of a specific electronic excitation.

SUPPLEMENTARY MATERIALS

The PDF contains the supplementary text providing additional details regarding PD-PEEM, the DFT calculations, and data analysis. Also included are Figure S1-S17, legend for Movie S1, and references [7, 22, 24, 37–40, 45–48].

Other supplemental materials include: Video of PEEM images vs θ_E for β'-In_2Se_3 (Movie S1).

ACKNOWLEDGMENTS

Funding: This work was funded by the Office of Basic Energy Sciences, U.S. Department of Energy (Grant No. DE-SC0021950). This work used facilities supported by the University of Chicago Materials Research Science and Engineering Center, which is funded by the National Science Foundation under award number DMR-2011854 and DMR-1420709, and resources provided by the University of Chicago's Research Computing Center. A portion of this research (DFT calculations) used

resources at the Center for Nanophase Materials Sciences, which is a U.S. Department of Energy Office of Science User Facility. P.P.J. acknowledges support from a MRSEC-funded Kadanoff-Rice fellowship (DMR-2011854 and DMR-1420709). L.L. acknowledges computational resources of the National Energy Research Scientific Computing Center, a DOE Office of Science User Facility supported by the Office of Science of the U.S. DOE under Contract No. DE-AC02-05CH11231. The authors thank C. Ophus from Lawrence Berkeley National Laboratory for helpful discussions regarding data analysis and K. Waters from the University of Chicago for assistance with manuscript preparation. **Author Contributions:** Conceptualization: JLS, PPJ, SBK; Methodology: JLS, PPJ, LL, SBK; Software: JLS, NM, PPJ, LL; Investigation: JLS, LK, PPJ; Resources: LK, LL, SBK; Visualization: JLS, SBK; Writing—original draft: JLS, SBK; Writing—review & editing: JLS, LK, PPJ, NM, LL, SBK; Funding acquisition: SBK; Supervision: SBK

[1] Z. Liu, T. Lu, J. Ye, G. Wang, X. Dong, R. Withers, and Y. Liu, Antiferroelectrics for Energy Storage Applications: a Review, Adv. Mater. Technol. **3**, 10.1002/admt.201800111 (2018).

[2] C. A. Randall, Z. Fan, I. Reaney, L. Chen, and S. Trolier-McKinstry, Antiferroelectrics: History, fundamentals, crystal chemistry, crystal structures, size effects, and applications, J. Am. Ceram. Soc. **104**, 3775 (2021).

[3] C. W. Ahn, G. Amarsanaa, S. S. Won, S. A. Chae, D. S. Lee, and I. W. Kim, Antiferroelectric Thin-Film Capacitors with High Energy-Storage Densities, Low Energy Losses, and Fast Discharge Times, ACS Appl. Mater. Interfaces **7**, 26381 (2015).

[4] M. M. Vopson and X. Tan, Four-State Anti-Ferroelectric Random Access Memory, IEEE Electron Device Lett. **37**, 1551 (2016).

[5] L. Liu, Y. Cai, X. Chen, Z. Liu, G. Yuan, and Y. Wang, Flexible multi-state nonvolatile antiferroelectric memory, J. Am. Ceram. Soc. **105**, 6232 (2022).

[6] A. K. Tagantsev, K. Vaideeswaran, S. B. Vakhrushev, A. V. Filimonov, R. G. Burkovsky, A. Shaganov, D. Andronikova, A. I. Rudskoy, A. Q. R. Baron, H. Uchiyama, D. Chernyshov, A. Bosak, Z. Ujma, K. Roleder, A. Majchrowski, J.-H. Ko, and N. Setter, The origin of antiferroelectricity in $PbZrO_3$, Nat. Commun. **4**, 2229 (2013).

[7] C. Xu, J. Mao, X. Guo, S. Yan, Y. Chen, T. W. Lo, C. Chen, D. Lei, X. Luo, J. Hao, C. Zheng, and Y. Zhu, Two-dimensional ferroelasticity in van der Waals β'-In_2Se_3, Nat. Commun. **12**, 3665 (2021).

[8] Q. N. Chen, Y. Ou, F. Ma, and J. Li, Mechanisms of electromechanical coupling in strain based scanning probe microscopy, Appl. Phys. Lett. **104**, 242907 (2014).

[9] Y. Kim, A. Kumar, A. Tselev, I. I. Kravchenko, H. Han, I. Vrejoiu, W. Lee, D. Hesse, M. Alexe, S. V. Kalinin, and S. Jesse, Nonlinear Phenomena in Multiferroic Nanocapacitors: Joule Heating and Electromechanical Effects, ACS Nano **5**, 9104 (2011).

[10] A. K. Tagantsev, L. E. C. Cross, and J. Fousek, *Domains in Ferroic Crystals and Thin Films* (Springer New York, NY, 2010).

[11] J. E. F. Gonzales, A. Ganzha, M. Kniazeva, D. Andronikova, A. Vakulenko, A. Filimonov, A. Rudskoy, C. Richter, A. Dasgupta, R. Gao, and R. Burkovsky, Thickness independence of antiferroelectric domain characteristic sizes in epitaxial $PbZrO_3/SrRuO_3/SrTiO_3$ films, J. Appl. Crystallogr. **56**, 697 (2023).

[12] B. Guzelturk, A. B. Mei, L. Zhang, L. Z. Tan, P. Donahue, A. G. Singh, D. G. Schlom, L. W. Martin, and A. M. Lindenberg, Light-Induced Currents at Domain Walls in Multiferroic BiFeO3, Nano Lett. **20**, 145 (2020).

[13] J. v. Landuyt, G. v. Tendeloo, and S. Amelinckx, Phase transitions in In_2Se_3 as studied by electron microscopy and electron diffraction, Phys. Status Solidi A **30**, 299 (1975).

[14] C. Manolikas, New results on the phase transformations of In_2Se_3, J. Solid State Chem. **74**, 319 (1988).

[15] W. Han, X. Zheng, K. Yang, C. S. Tsang, F. Zheng, L. W. Wong, K. H. Lai, T. Yang, Q. Wei, M. Li, W. F. Io, F. Guo, Y. Cai, N. Wang, J. Hao, S. P. Lau, C.-S. Lee, T. H. Ly, M. Yang, and J. Zhao, Phase-controllable large-area two-dimensional In_2Se_3 and ferroelectric heterophase junction, Nat. Nanotechnol. **18**, 55 (2023).

[16] S. Wan, Q. Peng, Z. Wu, and Y. Zhou, Nonvolatile Ferroelectric Memory with Lateral $\beta/\alpha/\beta$ In_2Se_3 Heterojunctions, ACS Appl. Mater. Interfaces **14**, 25693 (2022).

[17] F. Zhang, Z. Wang, L. Liu, A. Nie, Y. Gong, W. Zhu, and C. Tao, Atomic-Scale Visualization of Polar Domain Boundaries in Ferroelectric In_2Se_3 at the Monolayer Limit, J. Phys. Chem. Lett. **12**, 11902 (2021).

[18] Z. Chen, W. Fu, L. Wang, W. Yu, H. Li, C. K. Y. Tan, I. Abdelwahab, Y. Shao, C. Su, M. Sun, B. Huang, and K. P. Loh, Atomic Imaging of Electrically Switchable Striped Domains in β'-In_2Se_3, Adv. Sci. **8**, 2100713 (2021).

[19] Z. Zhang, J. Nie, Z. Zhang, Y. Yuan, Y. Fu, and W. Zhang, Atomic Visualization and Switching of Ferroelectric Order in β'-In_2Se_3 Films at the Single Layer Limit, Adv. Mater. **34**, 2106951 (2022).

[20] R. Vilaplana, S. G. Parra, A. Jorge-Montero, P. Rodriguez-Hernandez, A. Munoz, D. Errandonea, A. Segura, and F. J. Manjon, Experimental and Theoretical Studies on α-In_2Se_3 at High Pressure, Inorg. Chem. **57**, 8241 (2018).

[21] C. Zheng, L. Yu, L. Zhu, J. L. Collins, D. Kim, Y. Lou, C. Xu, M. Li, Z. Wei, Y. Zhang, M. T. Edmonds, S. Li, J. Seidel, Y. Zhu, J. Z. Liu, W.-X. Tang, and M. S. Fuhrer, Room temperature in-plane ferroelectricity in van der Waals In_2Se_3, Sci. Adv. **4**, eaar7720 (2018).

[22] X. Tao and Y. Gu, Crystalline-Crystalline Phase Transformation in Two-Dimensional In_2Se_3 Thin Layers, Nano Lett. **13**, 3501 (2013).

[23] X. Zheng, W. Han, K. Yang, L. W. Wong, C. S. Tsang, K. H. Lai, F. Zheng, T. Yang, S. P. Lau, T. H. Ly, M. Yang, and J. Zhao, Phase and polarization modulation in two-dimensional In_2Se_3 via in situ transmission electron microscopy, Sci. Adv. **8**, eabo0773 (2022).

[24] C. Xu, Y. Chen, X. Cai, A. Meingast, X. Guo, F. Wang, Z. Lin, T. W. Lo, C. Maunders, S. Lazar, N. Wang, D. Lei, Y. Chai, T. Zhai, X. Luo, and Y. Zhu, Two-Dimensional Antiferroelectricity in Nanostripe-Ordered

In_2Se_3, Phys. Rev. Lett. **125**, 047601 (2020).
[25] F. Crameri, Scientific colour maps, Zenodo 10.5281/ZENODO.5501399 (2021).
[26] F. Crameri, G. E. Shephard, and P. J. Heron, The misuse of colour in science communication, Nat. Commun. **11**, 5444 (2020).
[27] J. L. Collins, C. Wang, A. Tadich, Y. Yin, C. Zheng, J. Hellerstedt, A. Grubisic-Cabo, S. Tang, S.-K. Mo, J. Riley, E. Huwald, N. V. Medhekar, M. S. Fuhrer, and M. T. Edmonds, Electronic Band Structure of In-Plane Ferroelectric van der Waals β'-In_2Se_3, ACS Appl. Electron. Mater. **2**, 213 (2020), 1910.05969.
[28] F. Zhang, Z. Wang, J. Dong, A. Nie, J. Xiang, W. Zhu, Z. Liu, and C. Tao, Atomic-Scale Observation of Reversible Thermally Driven Phase Transformation in 2D In_2Se_3, ACS Nano **13**, 8004 (2019).
[29] J. Schaab, I. P. Krug, F. Nickel, D. M. Gottlob, H. Doğanay, A. Cano, M. Hentschel, Z. Yan, E. Bourret, C. M. Schneider, R. Ramesh, and D. Meier, Imaging and characterization of conducting ferroelectric domain walls by photoemission electron microscopy, Appl. Phys. Lett. **104**, 232904 (2014), 1405.2053.
[30] N. Barrett, J. E. Rault, J. L. Wang, C. Mathieu, A. Locatelli, T. O. Mentes, M. A. Niño, S. Fusil, M. Bibes, A. Barthélémy, D. Sando, W. Ren, S. Prosandeev, L. Bellaiche, B. Vilquin, A. Petraru, I. P. Krug, and C. M. Schneider, Full field electron spectromicroscopy applied to ferroelectric materials, J. Appl. Phys. **113**, 187217 (2013), 1806.04849.
[31] J. E. Rault, W. Ren, S. Prosandeev, S. Lisenkov, D. Sando, S. Fusil, M. Bibes, A. Barthélémy, L. Bellaiche, and N. Barrett, Thickness-Dependent Polarization of Strained BiFeO3 Films with Constant Tetragonality, Phys. Rev. Lett. **109**, 267601 (2012), 1210.3806.
[32] M. Ghidini, F. Maccherozzi, S. S. Dhesi, and N. D. Mathur, XPEEM and MFM Imaging of Ferroic Materials, Adv. Electron. Mater. **8**, 10.1002/aelm.202200162 (2022).
[33] N. Strkalj, M. Bernet, M. F. Sarott, J. Schaab, T. Weber, M. Fiebig, and M. Trassin, Stabilization and manipulation of in-plane polarization in a ferroelectric—dielectric superlattice, J. Appl. Phys **129**, 174104 (2021).
[34] J. M. Frost, K. T. Butler, F. Brivio, C. H. Hendon, M. v. Schilfgaarde, and A. Walsh, Atomistic Origins of High-Performance in Hybrid Halide Perovskite Solar Cells, Nano Lett. **14**, 2584 (2014), 1402.4980.
[35] X. Xiao, W. Li, Y. Fang, Y. Liu, Y. Shao, S. Yang, J. Zhao, X. Dai, R. Zia, and J. Huang, Benign ferroelastic twin boundaries in halide perovskites for charge carrier transport and recombination, Nat. Commun. **11**, 2215 (2020).
[36] X.-K. Wei, T. Sluka, B. Fraygola, L. Feigl, H. Du, L. Jin, C.-L. Jia, and N. Setter, Controlled Charging of Ferroelastic Domain Walls in Oxide Ferroelectrics, ACS Appl. Mater. Interfaces **9**, 6539 (2017).
[37] P. P. Joshi, R. Li, J. L. Spellberg, L. Liang, and S. B. King, Nanoimaging of the edge-dependent optical polarization anisotropy of black phosphorus, Nano Lett. **22**, 3180 (2022).
[38] A. Neff, F. Niefind, B. Abel, S. C. B. Mannsfeld, and K. R. Siefermann, Imaging Nanoscale Morphology of Semiconducting Polymer Films with Photoemission Electron Microscopy, Adv. Mater. **29**, 1701012 (2017).
[39] M. Sabooni, A. N. Nilsson, G. Kristensson, and L. Rippe, Wave propagation in birefringent materials with off-axis absorption or gain, Phys. Rev. A **93**, 013842 (2016).
[40] P. D. S. Haussühl, *Physical Properties of Crystals* (Wiley, 2007).
[41] A. Castellanos-Gomez, M. Buscema, R. Molenaar, V. Singh, L. Janssen, H. S. J. v. d. Zant, and G. A. Steele, Deterministic transfer of two-dimensional materials by all-dry viscoelastic stamping, 2D Mater. **1**, 011002 (2014).
[42] G. Kresse and J. Furthmüller, Efficient iterative schemes for ab initio total-energy calculations using a plane-wave basis set, Phys. Rev. B **54**, 11169 (1996).
[43] G. Kresse and D. Joubert, From ultrasoft pseudopotentials to the projector augmented-wave method, Phys. Rev. B **59**, 1758 (1999).
[44] J. P. Perdew, K. Burke, and M. Ernzerhof, Generalized gradient approximation made simple, Phys. Rev. Lett. **77**, 3865 (1996).
[45] J. H. Weaver, C. G. Olson, and D. W. Lynch, Optical investigation of the electronic structure of bulk Rh and Ir, Phys. Rev. B **15**, 4115 (1977).
[46] X. Ling, S. Huang, E. H. Hasdeo, L. Liang, W. M. Parkin, Y. Tatsumi, A. R. T. Nugraha, A. A. Puretzky, P. M. Das, B. G. Sumpter, D. B. Geohegan, J. Kong, R. Saito, M. Drndic, V. Meunier, and M. S. Dresselhaus, Anisotropic Electron-Photon and Electron-Phonon Interactions in Black Phosphorus, Nano Lett. **16**, 2260 (2016).
[47] F. Lyu, X. Li, J. Tian, Z. Li, B. Liu, and Q. Chen, Temperature-Driven α-β Phase Transformation and Enhanced Electronic Property of 2H α-In_2Se_3, ACS Appl. Mater. Interfaces **14**, 23637 (2022).
[48] A. Rodger and B. Nordén, *Circular Dichroism and Linear Dichroism* (Oxford University Press, 1997).